X-Ray Peak Broadening Analysis in $LaMnO_{3+\delta}$ Nano-Particles with RhombohedralCrystal Structure

A.Gholizadeh[a,*]

[a]*School of Physics, Damghan University (DU), Damghan, Iran.*

ARTICLE INFO

Article history:

Received 10 April 2015
Accepted 11 October 2015
Available online 30 September 2015

Keywords:

Manganite
Nano- Perovskite
Hexagonal to Rhombohedral
Lattice Conversion
Peak Broadening

ABSTRACT

In this work, structural and magnetic properties of the $LaMnO_{3+\delta}$ compound prepared by citrate precursor method and annealed in the presence of oxygen are investigated. The structural characterization of $LaMnO_{3+\delta}$ by X-ray powder diffraction and X'pert package and Fullprof program provides evidence for a rhombohedral structure (R-3c space group) confirmed by FTIR measurement as well. The magnetic measurements show a super-paramagnetic behavior of $LaMnO_{3+\delta}$ due to low values of the coercive field and remanance magnetization and also high value of saturation magnetization. In addition, a comparative study of the crystallite size of the compounds obtained from powder XRD is reported. The Williamson-Hall analysis, size-strain plot and Halder-Wagner methods were used to study the individual contributions of the crystallite sizes and lattice micro-strain to isotropic line broadening of all the reflection peaks of the $LaMnO_{3+\delta}$ compound. The results show that the Halder-Wagner method is more accurate, with all data points touching the fitting line better than in the other methods. The crystallite sizes estimated from XRD (30.86 nm) and particle size estimated from TEM method (36 nm) and also the magnetic core size (33.6 nm) estimated from magnetic measurement are in good agreement, while a little difference reflects a spherical shape of the nanoparticles.

1. Introduction

$LaMnO_3$ with perovskite structure is an insulator-antiferromagnetic at room temperature due to the absence of Mn^{4+} ions [1]. $LaMnO_3$ can be a semiconductor-ferromagnetic or metal-ferromagnetic compound depending on the presence of Mn^{4+} concentration [2]. With replacement of La^{3+} ions by bivalent element (Sr, Ca, …), trivalent ions Mn are converted to a mixture of Mn^{3+} ions and Mn^{4+}. The measurements reported on polycrystalline samples $La_{1-y}M_yMnO_3$ showed insulator-antiferromagnetic behavior in low and high values of y, and metal-ferromagnetic behavior in concentration $y \approx 1/3$ [3, 4]. In these compounds, the ferromagnetic-paramagnetic transition associated with a metal-insulator transition below the Curie temperature (100 <TC (K) <350) have been attributed to double-exchange intraction between the ions of Mn^{3+}-Mn^{4+} [5].

Also, previous studies [6-8] showed that stoichiometric $LaMnO_3$ should be prepared in the absence of oxygen, but sintering in ambient

Corresponding author:
*E-mail address:*gholizadeh@du.ac.ir(Ahmad Gholizadeh).

Also, previous studies [6-8] showed that stoichiometric $LaMnO_3$ should be prepared in the absence of oxygen, but sintering in ambient air or deposition in the presence of carrier-gas pressure (O_2) results in nonstoichiometric $LaMnO_{3+\delta}$ with formation of Mn^{4+} ions. Therefore, $LaMnO_3$ can be orthorhombic, rhombohedral or cubic depending on the Mn^{4+} concentration. When the Mn^{4+} concentration is about 0–12%, 18–30%, and more than 30%, $LaMnO_3$ becomes orthorhombic, rhombohedral, and cubic, respectively. Therefore, the presence of Mn^{4+} plays an important role in structural and magnetic properties of $LaMnO_3$.

Both the preparation technique and the crystal imperfections can affect the properties of nanostructures. Bragg's equation assumes that crystal is perfect and infinite and incident beam is perfectly parallel and monochromatic. However, actual experimental conditions are different from these assumptions, leading to various kinds of deviations from Bragg's condition. The peaks are not 'd' curves and they are broadened. There are also deviations from the assumptions involved in the generating powder patterns. For example, in a powder sample if the crystallite size be smaller than 0.5 mm, there are insufficient number of planes to build up a sharp diffraction pattern and consequently the peaks are broadened. Both crystallite size and lattice microstrain have effects on Bragg's peaks by increasing the peak width, intensity and shifting the 2θ peak position [9-10].

In this paper, we analyzed the XRD data of $LaMnO_{3+\delta}$ prepared by citrate precursor method using a commercial X'pert package and Fullprof program and tried to explain the structural and magnetic properties. In addition, a comparative study of the mean crystallite size of the compounds obtained from powder XRD is reported. The microstrain due to lattice deformation of the $LaMnO_{3+\delta}$ nanoparticles was estimated by the Williamson-Hall (W-H) analysis, size-strain plot (SSP) and Halder-Wagner (H-W) methods. The crystallite sizes results obtained by these methods are compared with the Scherer and also the particle size estimated from TEM and magnetic methods.

2. Experimental

2.1. Synthesis of the sample

The $LaMnO_{3+\delta}$ compounds were prepared by the citrate method using metal nitrate precursor in the presence of citric acid. Firstly, a solution containing 0.0124 mole of metal nitrates $La(NO_3)_3 6H_2O$, $Mn(NO_3)_2 \cdot 4H_2O$, and 0.0615 mole of citric acid, equal to the total number of moles of nitrate ions, was evaporated at 60°C overnight. The homogeneous sol-like substance was subsequently dried at 80°C overnight. The resulted spongy and friable materials were completely powdered and kept at 200 °C overnight. This precursor was then heated at 600 °C for 5 h to remove carbonaceous material. Then, the obtained materials were powdered again and subsequently calcined at 900°C to obtain the products.

2.2. Geometric characterization

XRD and TEM were used to obtain the textural parameters of the materials such as size, shape, composition, and crystal structure. The X-ray diffraction (XRD) pattern was recorded using a Bruker AXS diffractometer D8 ADVANCE with Cu-K_α radiation in the range of 2θ = 10-80° at room temperature. The XRD data was analyzed using a commercial X'pert package and Fullprof program.

XRD profile analysis is a simple and powerful method to evaluate the crystallite size and lattice microstrain. Two factors determine the breadth of Bragg's peak including crystallite size-dependent (β_C) and microstrain dependent broadening (β_S) effects, except for the instrument-dependent effect. To do an accurate analysis of the size and microstrain effects, at first, Instrumental broadening has to be subtracted using the undeformed silicon as a standard reference material to get the broadening effects due to the sample.

2.3. Magnetic characterization

The hysteresis loops at 10 K and also temperature dependence of magnetization between 10-400 K were examinedcarried out in a SQUID magnetometer (Quantum Design, Inc.). The magnetization curve in high fields can be usually fitted by law of approach to saturation [11]:

$$M(H) = M_S[1 - (a/H) - (b/H^2) - (c/H^3)] + \chi H + EH^{1/2} \quad [1]$$

Where M(H) is the magnetization at the field H M_S is the saturation magnetization explained by atomic theory, a is the inhomogeneity parameter, b is the factor which is proportional to K^2 (K is the anisotropy constant), and c is a factor proportional to K^3. The proportionality factors of b and c depend on the form of the anisotropy function and on the special symmetry of the lattice. On the other hand, χ is the susceptibility, and E is the spin wave factor.

3. Results and discussions

3.1. The XRD analysis

X-ray diffraction pattern of the $LaMnO_3$ compound is shown in Fig. 1. A small splitting of the peaks observed at ~33°, ~41°, ~58°, ~68° and ~78° is an indication of a rhombohedral system. The XRD data was analyzed using both the commercial X'pert High Score package and Fullprof program. Identification of the structure type using X'pert package confirms a perovskite structure without presence of impurity phases. The XRD pattern of the sample fits well with the diffraction pattern of a rhombohedral structure of $LaMnO_{3.15}$ (JCPDS, 320484).

Result of the rietveld analysis using Fullprof program indicates that all the diffraction peaks of the XRD pattern can be quite well indexed in rhombohedral structure (space group R-3c) with reference to hexagonal axes. Also, the obtained result indicates that the best fit with the least difference is carried out (see Fig. 1). To perform a rietveld refinement using Fullprof program we need good initial values for lattice parameters and the type of space group obtained from phase analysis of X'pert package. The pure manganite $La^{3+}Mn^{3+}O^{2-}{}_3$ is essentially antiferromagnetic [6] with an orthorhombic structure. $LaMnO_3$ can be orthorhombic, rhombohedral or cubic depending on the Mn^{4+} concentration. When the Mn^{4+} concentration is about 0–12%, 18–30%, and more than 30%, $LaMnO_3$ becomes orthorhombic, rhombohedral, and cubic, respectively. A recent study [6] showed that stoichiometric $LaMnO_3$ should be prepared in the absence of oxygen but sintering in ambient air results in nonstoichiometric $LaMnO_{3+\delta}$ with formation of Mn^{4+} ions larger than 20% and with rhombohedral structure. Consequently, for our sample $LaMnO_3$ annealed in the presence of oxygen, the room temperature structure is rhombohedral, which indicates that the percentage of Mn^{4+} is larger than 20%. This result is confirmed by the magnetic data presented later in this work.

The hexagonal cell is no longer primitive and has three times the volume of the rhombohedral cell. When the XRD pattern of a rhombohedral sample has been so indexed, i.e., with reference to hexagonal axes, and the true nature of the lattice determined, we usually want to know the lattice parameters ar and α of the rhombohedral unit cell. But the dimensions of the rhombohedral cell can be determined from the dimensions of the hexagonal cell, and this is an easier process compared to solving the rather complicated plane-spacing equation for the rhombohedral system. The first step is to analyze and index the XRD pattern on the basis of hexagonal axes using Fullprof program. Then, the parameters a_H and c and also unit cell volume V_r of the hexagonal cell are refined using Fullprof program are 5.497 Å, 13.322 Å and 348.73 Å^3, respectively. Finally, the parameters a_r, α, and unit cell volume V_r of the rhombohedral cell are determined from the refined parameters a_H, c, and V_H of the hexagonal cell using Fullprof program according to the following equations:

$$a_r = \frac{1}{3}\sqrt{3a_H^2 + c^2} \quad [2]$$

$$\sin\frac{\alpha}{2} = \frac{3}{2\sqrt{3+(c/a_H)^2}} \quad [3]$$

$$V_r = \frac{1}{3}V_H \quad [4]$$

The derived lattice parameters a (= b = c) and α (= β = γ), and unit cell volume Vr for rhombohedral structure are 5.458 Å, 60.473 ° and 116.243 Å^3, respectively.

It should be noted that if the c/a_H ratio of the hexagonal cell takes the special value of 2.45, the angle α of the rhombohedral cell will equal 60° and the bond angle B-O-B is 180°. Consequently, the lattice of points will be face-centered cubic (t is equal to 1). Also, the magnitude of the rotation of BO_6 can be

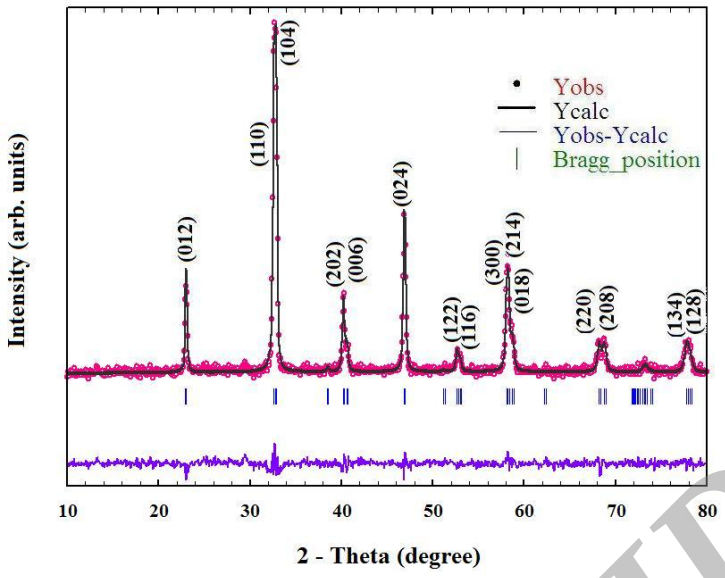

Fig. 1. Rietveld analysis of the X-ray diffraction pattern for $LaMnO_{3+\delta}$.

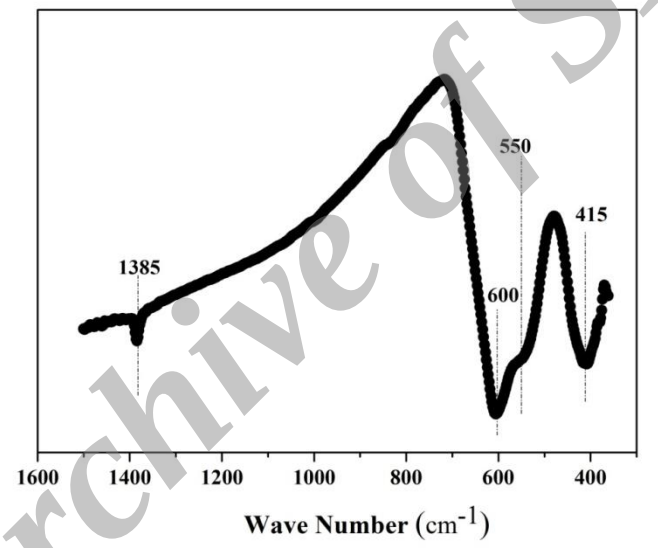

Fig. 2. FT-IR spectra for$LaMnO_{3+\delta}$.

evaluated from either the angle α of the rhombohedral unit cell or from the axial ratio c/aH of the hexagonal cell. As a result of the rotation (tilting), the B-O-B bond angle (≤180°) and α deviate from the ideal perovskite value. Notice that for trigonal angles α less than 60 degrees, the transformation can be achieved by an expansion along the body diagonal [111] of the rhombohedral or along the c-axis [001] of the hexagonal, while for trigonal angles greater than 60 degrees, it is a contraction the body diagonal [111] of the rhombohedral or along the c-axis [001] of the hexagonal. Therefore, the obtained value of angle α higher than 60˚ means BO_6 octahedron is slightly compressed along the (hexagonal c axis) rhombohedral (111) axis with respect to cubic structure.

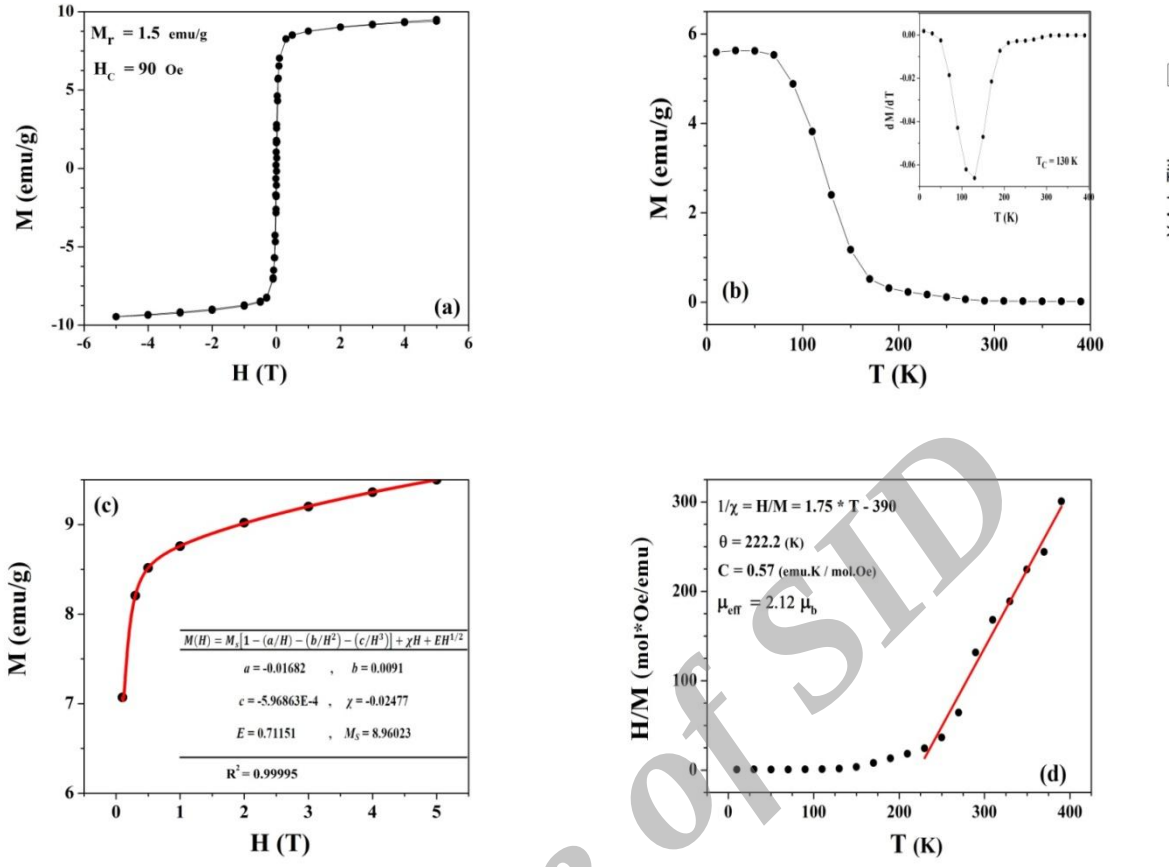

Fig. 3. (a) The hystersis loop of magnetization versus applied filed at 10 K, (b) The magnetization curves versus temperature measured under applied magnetic field 0.1T, (c) Fitted curve of M-H obtained from the law of approach to saturation (d) The fitting of temperature dependence of the inverse susceptibility (H/M) for paramagnetic phase of $LaMnO_{3+\delta}$ samples.

Fig. 2 shows the FTIR spectrum of $LaMnO_{3+\delta}$. The presence of metal oxygen bonds, i.e. symmetrical lengthening of the O-B-O and asymmetrical lengthening of the B-O bond of the octahedron BO_6 structures could be revealed from the peaks at 415 and 600 cm-1, respectively [12]. The widening of the 600 cm-1 band and/or the appearance of a shoulder at 550 cm-1 and the peak at 410 cm-1 are characteristic of a rhombohedral structure with lower symmetry. The narrow band at 1385 cm-1 might correspond to the CO_3^{2-} groups.

3.2. The magnetic properties

The hysteresis loop of $LaMnO_{3+\delta}$ is shown in Fig. 3a. The curve of M_H, S-shaped hysteresis loop show the coercivity field H_C, remanance magnetization M_r and the saturation magnetization M_S. H_C (= 90 Oe) and Mr (= 1.5 emu/g) are obtained from intersection of the hysteresis loop with the axis x and the axis y, respectively. Also, temperature dependence of magnetization in the range 5-400 K under applied magnetic field 0.1T for $LaMnO_{3+\delta}$ is shown in Fig. 3b. The Curie temperature obtained from the critical point in the derivative of the M-T curves is 130 K (see inset of Fig. 3b).

Result of fitting of M_H by law of approach to saturation indicates that the best fit with the least difference is carried out (see Fig. 3c). The calculated values of M_S, a, b, c, χ and E are written on Fig. 3c. The low values of H_C and M_r and also the high value of M_S (= 8.96 emu/g) show super-paramagnetic behavior of $LaMnO_{3+\delta}$. In fact, the high slope of the

magnetization curve in the range of high magnetic fields seems to indicate the existence of a superparamagnetic behavior of the smaller ferromagnetic particles.

The pure manganite $La^{3+}Mn^{3+}O^{2-}_3$ (x = 0) is essentially antiferromagnetic [12] with an orthorhombic structure, while in our case there is a ferromagnetic component with low coercive field and large magnetization values. A recent study [6] showed that stoichiometric $LaMnO_3$ should be prepared in the absence of oxygen, but sintering in ambient air results in nonstoichiometric $LaMnO_{3+\delta}$ with formation of Mn^{4+} ions larger than 20%. For our sample $LaMnO_3$ annealed in the presence of oxygen, the room temperature structure is rhombohedral, which indicates that the percentage of Mn^{4+} is larger than 20%. Therefore, magnetization values observed in the studied $LaMnO_3$ sample can be related to double exchange of Mn^{4+}- Mn^{3+}.

The analysis of high-temperature susceptibilities (M/H) of the samples was performed using the Curie–Weiss (CW) law:

$$\chi(T) = \frac{C}{T-\theta} \quad [5]$$

Table 1. The values of $2\Theta$and β_{hkl} ofFitted 15 Diffraction Lines for $LaMnO_{3+\delta}$ and the values of crystallite size obtained from Scherrer method

(hkl)	2Θ (˚)	β_{hkl} (˚)	$D_{Scherrer}(nm)$
012	22.9418	0.293	28.90
110	32.5483	0.2655	32.56
104	32.7893	0.2651	32.63
202	40.1961	0.2617	33.77
006	40.5976	0.2621	33.76
024	46.874	0.2744	32.96
122	52.6431	0.2974	31.13
116	52.9697	0.2991	31.00
300	58.0746	0.3288	28.87
214	58.2278	0.3298	28.80
018	58.6857	0.3328	28.60
220	68.1763	0.4091	24.49
208	68.7357	0.4144	24.26
134	77.7358	0.5094	20.92
128	78.1349	0.5141	20.78

Where $C\,(=({}^{1}/_{3k_B})\mu_{eff}^2$, $\mu_{eff}(S)(=\mu_B g\sqrt{S(S+1)}$ and θ are the Curie constant, the effective magnetic moment and the paramagnetic CW temperature, respectively. The fitting of the experimental (H/M)-(T) dependence on the linear function ${}^{1}/_{\chi(T)}$from the above equation has shown that temperature dependence of the inverse susceptibility is linear for the paramagnetic phase and obeys the CW law (see Fig. 3d). The CW temperatures, θ, calculated as a result of a fitting of CW law to the experimental data, was found to have a positive sign that is indicative of dominant ferromagnetic interactions. The C, θ, T_C and μ_{eff} values for the $LaMnO_{3+\delta}$ are shown on Fig 3d.
In the systems with mixed valency of Mn^{3+} and Mn^{4+} ions, the total magnetic moment (μ_{tot}) can be written in the form of:

$$\mu_{tot}^2 = x\mu_{eff}^2(S_1) + (1-x)\mu_{eff}^2(S_2) \qquad [6]$$

where $S_1 = 1$ and $S_2 = 3/2$ are values of the spin of Mn^{3+} and Mn^{4+} ions, respectively, x = 0.8 is the Mn3+ concentration supposed in $LaMnO_{3+\delta}$ having rhombohedral structure according to structural results and g-factor is equal to 2. The high value of the total moment of μ_{tot} = 3.044 μ_B was obtained. The μtot value is between the spin-only values for Mn^{3+} (2.8 μ_B) and Mn^{4+} (3.87 μ_B) ions. In our case, the effective number of Bohr magnetons (μ_{eff}) determined experimentally for $LaMnO_{3+\delta}$ is smaller than the total effective moment value (μ_{tot}). Similar situation was observed in Ref. [6] and was explained by the presence of the magnetic Mn^{3+} and Mn^{4+} clusters.

3.3 Determination of crystallite size, microstrain, and particle size

In below, a comparative study of the mean crystallite size of $LaMnO_{3+\delta}$ obtained from powder XRD is reported. The microstrain due to lattice deformation of the $LaMnO_{3+\delta}$ nanoparticles was estimated by W-H, SSP and H-W methods and the crystallite sizes results obtained by these methods are compared with the Scherer, magnetic and TEM methods. In all these methods, the values of β_{hkl} (the full-width at half-maximum (FWHM) of the diffraction peaks) and θ are selected from the results obtained from rietveld refinement using Fullprof program corresponding to the 15

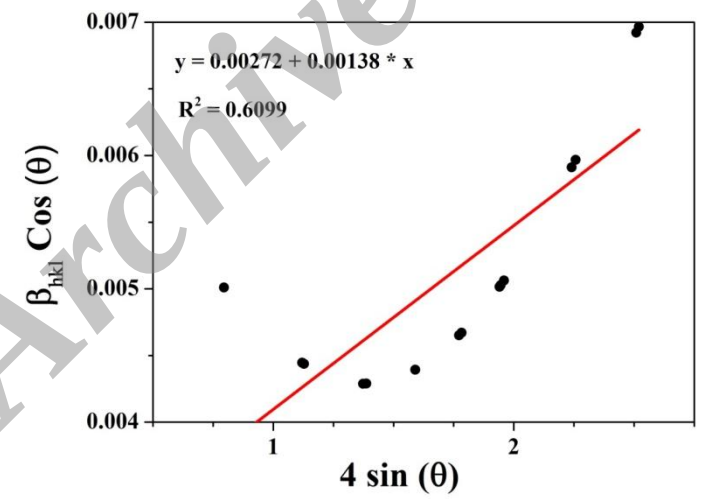

Fig. 4. The W-H analysis of $LaMnO_{3+\delta}$. Fit to the data, the microstrain is extracted from the slope and the crystalline size is extracted from the y-intercept of the fit.

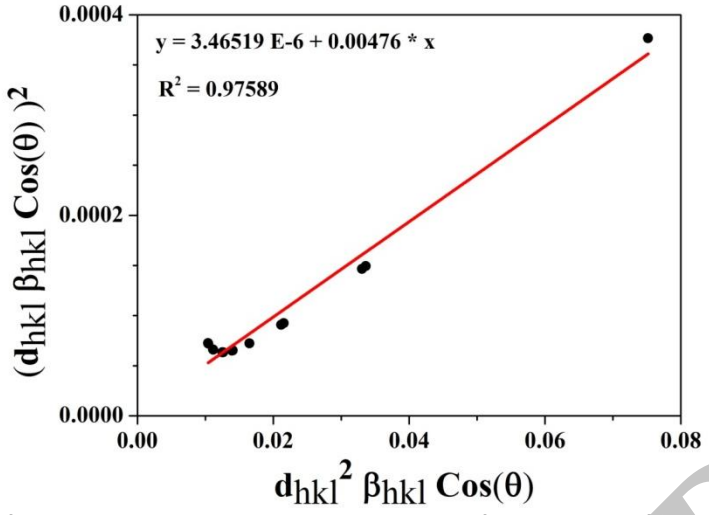

Fig. 5. The SSP plot of $LaMnO_{3+\delta}$. The crystallite size is achieved from the slop of the liner fitted data and the root of y-intercept gives the microstrain

strongest peaks of $LaMnO_{3+\delta}$ shown in Fig. 1. Also, the values of $dhkl$ (the distance between adjacent planes in the Miller indices (hkl)) are calculated from the Bragg's equation, $2d_{hkl}\sin\theta = \lambda$, with λ = 1.5404 Å.

3.3.1. The Scherrer method

The instrumental corrected broadening [13] βhkl (= βC)was estimated by using Gaussian function:

$$\beta_C^2 = \beta_{hkl}^2 = \beta^2 - \beta_I^2 \quad [7]$$

Also, Scherrer's equation as follows:

$$\beta_{hkl} = \frac{K\lambda}{D\cos\theta} = \beta_C \quad [8]$$

Shows the broadening of the XRD pattern which is attributed to the crystallite size-induced broadening. Here, βhkl is the full-width at half maximum (FWHM) corresponding to the 15 strongest peaks of $LaMnO_{3+\delta}$ shown in Fig. 1, K is the Scherrer constant equal to 0.94, D is the crystallite size, λ the wavelength of the X-ray, and Θ is the Bragg's angle.

In this method, the increase of peak broadening is due to the decrease of the crystallite size. The Scherrer's formula is used for the determination of the crystallite size from Gaussian line profiles. The formula is not expected to be valid for very small crystallite sizes (<10 nm).

The crystallite size (D) of the 15 strongest peaks was extracted from the Scherrer method are written in Table 1. The crystallite sizes obtained from smaller diffraction angles are more accurate.

3.3.2. The Williamson-Hall method

In the W-H method, the information on microstrain (ε) and the crystallite size (D) of $LaMnO_{3+\delta}$ have been obtained from βhkl by using W-H relation. Microstrain broadening in the W-H method is defined as follows [14]:

$$\beta_S = 4\varepsilon\ tan\,\theta \quad [9]$$

Separating crystallite size broadening and microstrain broadening:

$$\beta_{hkl} = \beta_C + \beta_S = \frac{K\lambda}{D\cos\theta} + 4\varepsilon\ tan\ \theta \quad [10]$$

Rewriting Eq. (10), Formula for Williamson-Hall method is as follow [15]:

$$\beta_{hkl}cos\theta = \left(\frac{K\lambda}{D}\right) + (4\varepsilon\ sin\ \theta) \quad [11]$$

Where K is the Scherrer constant or the shape coefficient given as 0.94 for spherical particles and ε is the internal microstrain.

In this method, the plot of $\beta_{hkl}cos\theta$(axis-y) versus 4sinθ (axis-x) corresponding to the 15 strongest peaks of $LaMnO_{3+\delta}$ shown in Fig. 1 is a straight line (see Fig. 4). The slope and intercept of linearly fitted data give amounts of micro-strain (ε) and crystallite size $D_{W\text{-}H}$, respectively.

The negative microstrain may be caused by lattice contraction. Basically, the larger the intercept result the smaller the crystallite size,

and the larger the slope result the larger the microstrain. Intercept with origin means D is infinity or broadening is only due to microstrain broadening and zero slope means horizontal line with no microstrain or broadening is only due to crystallite size broadening. The value of $D_{W\text{-}H}$ is not true due to very low value of R^2.

3.3.3. The size-strain plot method

The information on microstrain (ε) and the crystallite size (D) of $LaMnO_{3+\delta}$ have been obtained from βhkl and planar spacing d_{hkl} (the distance between adjacent planes in the set (h k l)) by using size-strain plot (SSP) method. The SSP method is more accurate, especially at higher diffraction angles. Therefore, the crystallite size and lattice strain of the sample was calculated using the size-strain plot (SSP) method. In this method, the peak broadening due to the lattice strain is estimated from $\varepsilon = \beta_S/\tan\theta$ [16]. Therefore, the total broadening is obtained from:

$$\beta_{hkl} = \beta_C + \beta_S \quad [12]$$

According to the SSP method, the relation between lattice strain and crystallite size is given by [17]:

$$(d_{hkl}\beta_{hkl}cos\theta)^2 = (K/D)\left(d_{hkl}^2\beta_{hkl}cos\theta\right) + (\varepsilon/2)^2 \quad [13]$$

Where K is the shape coefficient given as 3/4 for spherical particles.

In the SSP method, the plot of $(d_{hkl}\beta_{hkl}cos\theta)^2$ (axis y) versus $\left(d_{hkl}^2\beta_{hkl}cos\theta\right)$(axis-x) corresponding to the 15 strongest peaks of $LaMnO_{3+\delta}$ shown in Fig. 1, is a straight line (see Fig. 5). The crystallite size is determined from the slope of the linearly fitted data and the root of the y-intercept gives the microstrain.

Table 2. The values of crystallite size and microstrain of $LaMnO_{3+\delta}$ obtained from Williamson-Hall (W-H) analysis, size-strain plot (SSP) and Halder-Wagner (H-W) methods and also particle sizes calculated by magnetic and TEM measurments.

D_{W-H} (nm)	ε_{W-H} (no unit) $*10^3$	D ssp (nm)	$\varepsilon_{ssp}*10^3$ (no unit)	D_{H-W} (nm)	ε_{H-W} (no unit) $*10^3$	D_{TEM} (nm)	D_{mag} (nm)
53.23	1.380	15.75	3.723	30.86	0.616	36	33.6

3.3.4. The Halder-Wagner method

The information on microstrain ($\varepsilon_{H\text{-}W}$) and the crystallite size ($D_{H\text{-}W}$) of $LaMnO_{3+\delta}$ have been obtained from βhkl and planar spacing d_{hkl} (the distance between adjacent planes in the set (h k l)) by using H-W method. Halder and Wagner have given an approximation to the integral breadth of a Voigt function as [18]:

$$\beta_{hkl}^2 = \beta_L\beta_{hkl} + \beta_G^2 \quad [14]$$

Where β_L and β_G are the Lorentzian and Gaussian components, respectively. In H-W method, the crystallite size and strain profiles are described by the Lorentzian and the Gaussian function, respectively. Consequently, we have [19]:

$$(\beta_{hkl}^*/d_{hkl}^*)^2 = (1/D)\left(\beta_{hkl}^*/{d_{hkl}^*}^2\right) + (\varepsilon/2)^2 \quad [15]$$

Where $\beta_{hkl}^* = \beta_{hkl}cos\theta/\lambda$ and $d_{hkl}^* = 2sin\theta/\lambda$.

In H-W method, the plot of $(\beta_{hkl}^*/d_{hkl}^*)^2$ (axis y) versus $\left(\beta_{hkl}^*/{d_{hkl}^*}^2\right)$ (axis-x) corresponding to the 15 strongest peaks of LaMnO3+δ shown in Fig. 1 is a straight line with a positive slope and a nonzero y-intercept (see Fig. 7). The crystallite size is determined from the slope inverse of the linearly fitted data and the root of the y-intercept gives the microstrain, respectively.

The results of crystallite size and microstrain of $LaMnO_{3+\delta}$ estimated by the Scherrer, W-H, SSP and H-W methods are summarized in Table 2. All the methods show that line broadening was essentially isotropic. The W-H method supposes that ‘‘crystallite size” profile and the ‘‘microstrain” profile contribute to the

line broadening with Lorentzian profiles but in both of the S-S and H-W methods are assumed that the ‘‘crystallite size” profile is described by a Lorentzian function and the “microstrain” profile by a Gaussian function. However, compared to the Scherrer and W-H methods, both of the S-S and H-W methods have the advantage that less weight is given to data from reflections at high angles, where the precision is usually lower. For this reason, in the W-H method it is suggested that the smaller angle peaks should be used to separate β_C and β_S.

The values of average crystallite size of $LaMnO_{3+\delta}$ obtained from the different models are less similar, implying that the inclusion of microstrain in various forms has a very large effect on the average crystallite size of

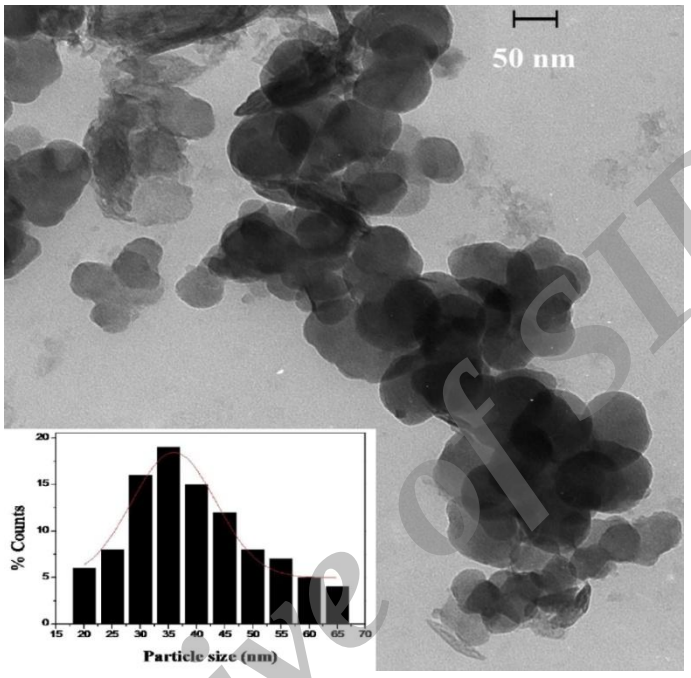

Fig. 6. TEM micrographs and size distribution histograms for $LaMnO_{3+\delta}$

$LaMnO_{3+\delta}$. However, looking at the values of R2 written inset of Figs. 4-6, we can observe that the H-W method is more accurate, with all data points touching the fitting line. Also, this method has minimum of the microstrain. Therefore, one method is more accurate which the value of R^2 is near 1 or in other words, data points of x-y are more touching the fitting line.

3.3.5. Particle size from TEM method

TEM micrographs and particle size distribution of $LaMnO_{3+\delta}$ is shown in Fig. 6. Size distribution histograms are fitted by using a log-normal function as follow:

$$P(d) = \frac{1}{D\sigma_d\sqrt{2\pi}} \exp\left\{-\frac{1}{2\sigma_d^2}\ln^2\left(\frac{D}{D_{TEM}}\right)\right\} \quad [16]$$

Where σ_d is the standard deviation of the diameter and DTEM is the mean diameter obtained from the TEM results (see the inset of Fig. 6). The mean diameter of particle size DTEM calculated by TEM method is 36 nm.

The $D_{W\text{-}H}$ is more than D_{TEM} and this is not true as a particle size is equal or greater than the crystallite size. It is interesting that the value of the crystallite size calculated by the H-W method is nearly similar to the mean diameter of the particle size D_{TEM} calculated by TEM method due to the regular shape of nanoparticles with spherical morphologies which is observed in the TEM micrograph [8].

3.3.6. Particle size from magnetic measurement

We evaluate the particle size distributions of $LaMnO_{3+\delta}$ from the analysis of magnetization

curves, and the results are compared with those estimated from TEM image and XRD analysis. Also, the M–H curve is well fitted with the size distributed Langevin function [20]:

$$M(D,H)=\sum M_i V_i f(d_i)L(x_i) \quad [17]$$

Where M_i and V_i, are magnetization and volume of ith particle, respectively and $f(di)$ is the log-normal function as follow:

$$f(d_i)=\frac{1}{\sqrt{2\pi}\ln\sigma}exp\left\{-\frac{(\ln d_i-\ln d_m)^2}{2\ln^2\sigma}\right\} \quad [18]$$

Where the parameters d_i, d_m and σ represent the diameter of ith particle, the statistical median and the geometric standard deviation, respectively. Also, $L(x_i)$ is the Langevin function:

$$L(x_i)=coth\ x_i-\frac{1}{x_i} \quad [19]$$

Where, x_i is defined as $x_i=\frac{\mu_i H}{k_B T}=\frac{M_i H}{k_B T}\frac{4\pi}{3}(\frac{d_i}{2})^3$.

The average diameter from magnetic measurement, which is denoted as D_{mag} hereafter, is expressed as:

$$D_{mag}=\frac{\sum_{i=1}^{n}\{d_i f(d_i)\}}{n} \quad [20]$$

Fitting of M/M_S curve versus H/T at 10 K with the size distributed Langevin function for LaMnO3+δ, results the magnetic core size as shown in Fig. 8. In this method, the average diameter of the $LaMnO_{3+\delta}$ nanoparticles is obtained as 33.6 nm and is in good agreement with the crystallite size estimated from Scherrer, H-W and TEM methods. Also, the magnetic diameter D_{mag} smaller than D_{TEM} reflects a very thin magnetically dead layer on the surface of the nanoparticles.

4. Conclusion

The structural and magnetic characterization of $LaMnO_{3+\delta}$ prepared by citrate precursor method was investigated by X-ray powder diffraction and FTIR measurements. The results of X'Pert package and Fullprof program on XRD pattern and also analysis of FTIR are evidences for a rhombohedral structure (R-3c space group). The magnetic measurements show the presence of the magnetic Mn^{3+} and Mn^{4+} clusters due to sintering in ambient air. The super-paramagnetic behavior of $LaMnO_{3+\delta}$ can be related to low values of the coercive field and remanance magnetization and also high value of the saturation magnetization. The results of crystallite size and microstrain of $LaMnO_{3+\delta}$compound estimated by the Scherrer, W-H, SSP and H-W methods show that the H-W method is more accurate, in which the value of R^2 is near 1 with all data points touching the fitting line better than in the other methods. Also, the crystallite size D_{H-W} similar to the particle size D_{TEM} and D_{mag} is a result of the regular shape of nanoparticles with spherical morphologies observed in the TEM micrograph.

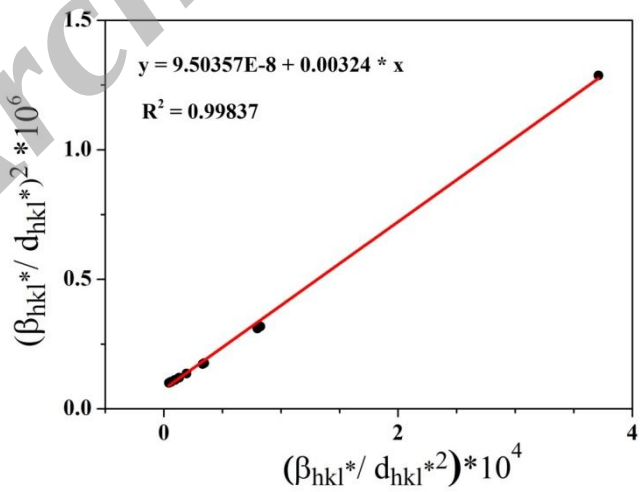

Fig. 7. The H-W plot of $LaMnO_{3+\delta}$. The *y*-intercept gives the mean value of the microstrain and the slope gives the crystallite size

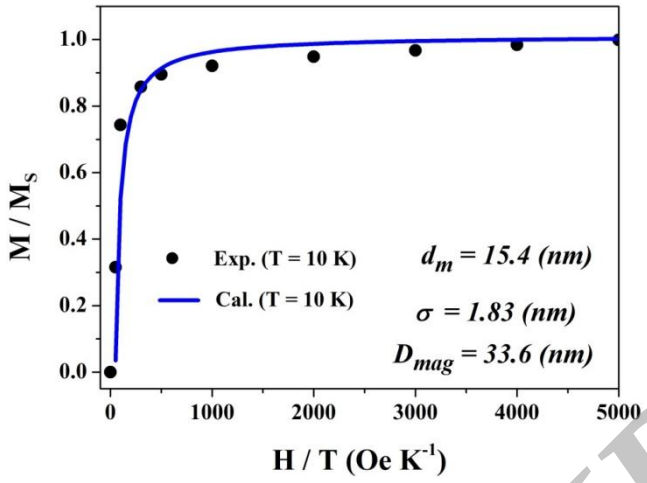

Fig. 8. Normalized magnetization (M/M_S) versus applied field divided by temperature (H/T) curves for $LaMnO_{3+\delta}$. Solid circles represent the experimental data for T = 10 K. The solid curve represents the calculation which gives the best fit to experiments

Acknowledgment

The author wishes to thank Frances Hellman, University of California-Berkeley, for her help in magnetic measurements.

References

1. M. A. Peña, J. L. G. Fierro, Chemical Structures and Performance of Perovskite Oxides, Chem. Rev., Vol. 101, 2001, pp.1981-2017.
2. R.G. Shetkar, A.V. Salker, Electrical, Magnetic and Catalytic Investigations on Some Manganite Perovskites Prepared by Combustion Method, J. Mater. Sci. Technol., Vol. 26, 2010, pp. 1098-1102.
3. C. Zener, Interaction Between the d Shells in the Transition Metals, J. Phys. Rev., Vol. 81, 1951, pp. 440-444.
4. J. B. Goodenough, Theory of the Role of Covalence in the Perovskite-Type Manganites [La, M(II)]MnO_3, J. Phys. Rev., Vol. 100, 1955, pp. 564-573.
5. M. B. Salamon, M. Jaime, The physics of manganites: Structure and transport, Rev. Mod. Phys., Vol. 73, 2001, pp. 1-28.
6. Y.D. Zhao, J. Park, R. J. Jung, H. J. Noh, and S. J. Oh, Structure, magnetic and transport properties of $La_{1-x}Bi_xMnO_3$, J. Magn. Magn. Mater., Vol. 280, 2004, pp. 404–411.
7. M. Lotfi, A. Gholizadeha, and A. Malekzadeh, Structural and Redox Properties of the $La_{1-x}Sr_xMn_{0.5}Co_{0.5}O_3$ (x = 0.0, 0.1, 0.2, 0.3, 0.4, 0.5) Nano-Catalysts for Carbon Monoxide Oxidation, Journal of Advanced Materials and Processing, Vol. 2, No. 4, 2014, pp. 65-70.
8. E. Frozandeh-Mehr, A. Malekzadeh, M. Ghiasi, A. Gholizadeh, Y. Mortazavi, and A. Khodadadi, Effect of partial substitution of lanthanum by strontium or bismuth on structural features of the lanthanum manganite nanoparticles as a catalyst for carbon monoxide oxidation,Catal. Commun., Vol. 28, 2012, pp. 32–37.
9. R. Yogamalara, R. Srinivasan, A. Vinu, K. Ariga, and A. C. Bose, X-ray peak broadening analysis in ZnO nanoparticles, Solid State Commun., Vol. 149, 2009, pp. 1919-1923.
10. A. Khorsand Zak, W.H. Abd. Majid, M.E. Abrishami, and R. Yousefi, X-ray analysis of ZnO nanoparticles by Williamson-Hall and sizee strain plot methods, Solid State Sci., Vol. 13, 2011, pp. 251-256.
11. R. Groessinger, A Critical Examination of the Law of Approach to Saturation, phys. stat. sol. (a), Vol. 66, 1981, pp. 665-674.
12. G. Pecchi, C. Campos, O. Peña, and L. E. Cadus, Structural, magnetic and catalytic properties of perovskite-type mixed oxides $LaMn_{1-x}Co_xO_3$ (x = 0.0, 0.1, 0.3, 0.5, 0.7, 0.9,

1.0), J. Mol. Catal. A: Chem., Vol. 282, 2008, pp. 158–166.
13. K. D. Rogers, P. Daniels, An X-ray diffraction study of the effects of heat treatment on bone mineral microstructure, Biomaterials, Vol. 23, No. 12, 2002, pp. 2577.
14. A. R. Stokes, A. J. C. Wilson, The diffraction of X rays by distorted crystal aggregates – I, Proc. Phys. Soc., Vol. 56, 1944, pp. 174.
15. G. K. Williamson, W. H. Hall, X-raylinebroadeningfromfildaluminiumand wolfram, Acta Metall., Vol. 1, 1953, pp. 22.
16. B. D. Cullity, Elements of X-ray Diffraction, Addison-Wesley Publishing Company Inc., California, 1956.
17. M. A. Tagliente, M. Massaro, Strain-driven (002) preferred orientation of ZnO nanoparticles in ion-implanted silica,Nucl. Instrum. Methods. B, Vol. 266, 2008, pp. 1055–1061.
18. N. C. Halder, N. C. J. Wagner, Separation of particle size and lattice strain in integral breadth measurements, Acta Crystallogr., Vol. 20, 1966, pp. 312.
19. J. E. Langford, International Conference Accuracy in Powder Diffraction II, National Institut of Standards and Technology, Special Publication 846, Gaithersburg, MD, USA, 1992, pp. 145.
20. K. Yakushiji, S. Mitani, K. Takanashi, J-G. Ha, and H. Fujimori, Composition dependence of particle size distribution and giantmagnetoresistance in Co-Al-O granular films, J. Magn. Magn. Mater. 212(2000)75.